Measurement of needle and armature dynamics in a gasoline direct injector by high-speed neutron imaging

M.L. Wissink[1], T.J. Toops[1], D.A. Splitter[1], E.J. Nafziger[1], C.E.A. Finney[1], H.Z. Bilheux[2], and Y. Zhang[2]

[1]Oak Ridge National Laboratory, Energy Science and Technology Directorate, Oak Ridge, TN 37830

[2]Oak Ridge National Laboratory, Neutron Sciences Directorate, Oak Ridge, TN 37830

E-mail: wissinkml@ornl.gov

Abstract. In modern spark ignition engines, precise delivery of fuel with gasoline direct injection has become increasingly important in the effort to meet ever stricter efficiency and emissions regulations. Use of multiple small close-coupled injections has become more common in attempt to precisely control fuel distribution in the cylinder, but these strategies are hindered by nonlinear injection effects due to operation in the ballistic region of the solenoid-operated valve and due to armature bounce at the end of injection. Understanding the internal dynamics of the injector is crucial to minimizing and controlling non-linearity and shot-to-shot variation, but the experimental techniques available to date are capable only of tracking the position of either the top of the needle (via laser sensors or by monitoring current and voltage in the solenoid coil) or the bottom of the needle (via transparent nozzles or high-speed x-ray imaging). A complete picture of the axial and radial motion of valve needle has until now remained elusive. In this work, we present high-speed ensemble neutron transmission imaging of an entire 8-hole gasoline direct injector operating at 200 bar, allowing for both visualization and quantification of the actuation dynamics including lift and wobble of the valve ball, oscillation and bending of the valve needle, lift, rocking, and bounce of the armature, compression of the springs, and radial swelling of the solenoid during energization. Because neutrons offer high penetration through the metal injector while also being sensitive to the ^{1}H nuclei in fuel molecules, it is also possible to simultaneously see the fluid dynamics of the injection process, including filling of the sac volume, emanation of the spray through the nozzle holes and into the downstream gas, and the formation and evolution of fuel films on the tip of the injector and the walls of the spray container.

Notation

CT	*computed tomography*
DOE	*Department of Energy*
EOE	*end of energization*
GDI	*Gasoline direct injection*
HFIR	*High Flux Isotope Reactor*
MCP	*microchannel plate*
ORNL	*Oak Ridge National Laboratory*
PM	*particulate matter*
SOE	*start of energization*

1. Introduction

Over the last decade, spark ignition engines have undergone a shift toward downsizing, turbocharging, and gasoline direct injection (GDI) in order to meet increasingly stringent fuel economy regulations [1]. GDI offers multiple benefits including charge cooling and the ability to tailor the delivery of the fuel into the cylinder to optimize the combustion process. However, high spray penetration with GDI can lead to wall films which cause high levels of particulate matter (PM), especially during cold start [2].

One method to reduce PM formation is to split the fuel delivery into multiple smaller injections, which reduces the spray penetration and formation of wall films [3]. However, this leads to additional

This manuscript has been authored by UT-Battelle, LLC, under contract DE-AC05-00OR22725 with the US Department of Energy (DOE). The US government retains and the publisher, by accepting the article for publication, acknowledges that the US government retains a nonexclusive, paid-up, irrevocable, worldwide license to publish or reproduce the published form of this manuscript, or allow others to do so, for US government purposes. DOE will provide public access to these results of federally sponsored research in accordance with the DOE Public Access Plan (http://energy.gov/downloads/doe-public-access-plan).

challenges. The use of multiple injections requires a smaller minimum injection quantity, while the trend towards downsizing and turbocharging requires a larger maximum injection quantity to meet the higher load per cylinder. It is also generally desirable to place the multiple injections as close together as possible to achieve a homogenous fuel–air mixture before combustion. These requirements can lead to operation in the nonlinear range of the injector due to short injections which end before the needle is fully open and due to close-coupled injections which occur in the ballistic region of the solenoid-operated valve.

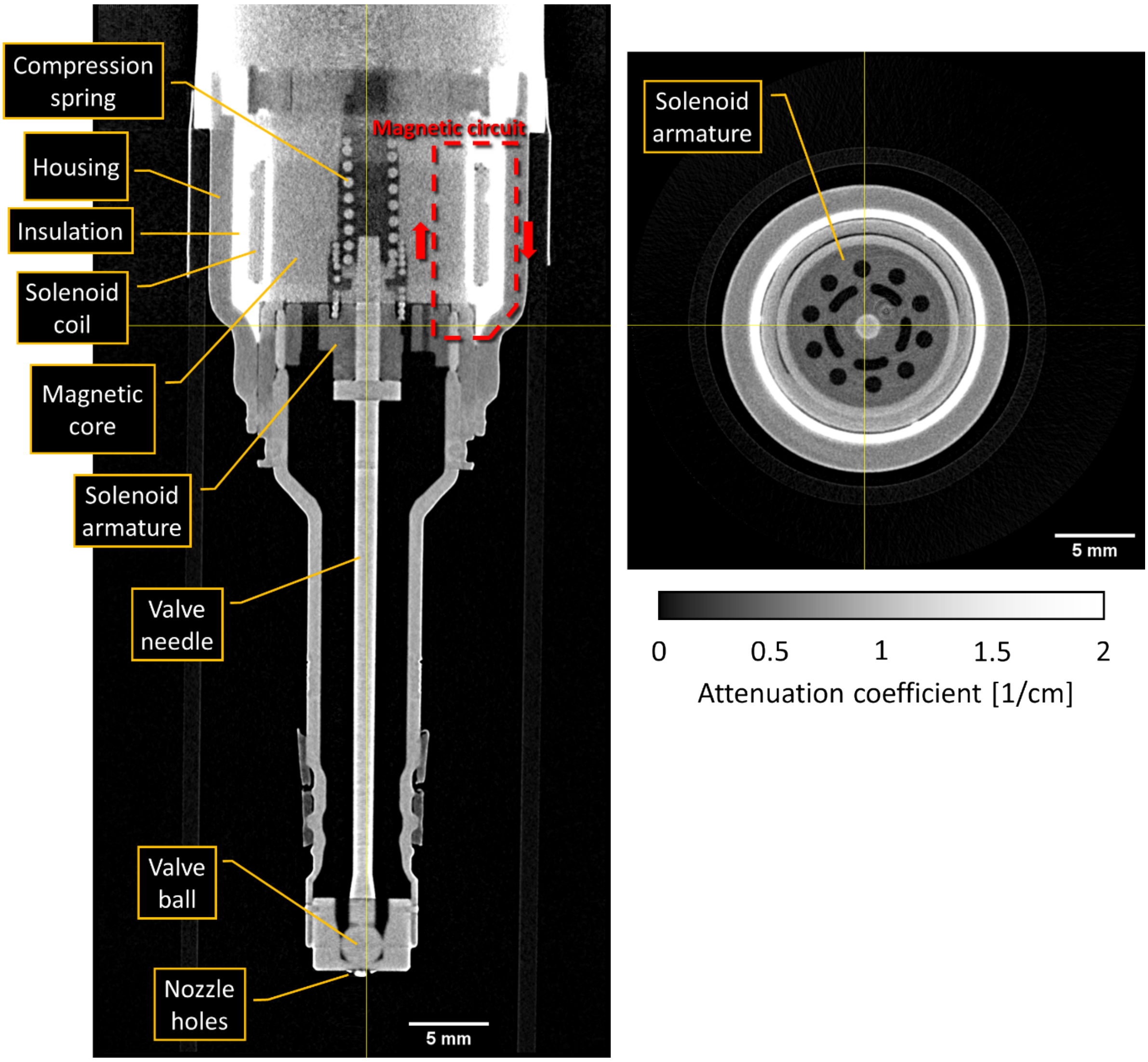

Figure 1. Sagittal and transverse cut planes from neutron CT reconstruction of a gasoline direct injector show internal components and geometry

Cut planes from a neutron computed tomography (CT) reconstruction of an 8-hole gasoline direct injector [4], shown in **Figure 1**, illustrate its internal features and construction. Fuel flow is controlled by a valve ball, which is compressed against the valve seat by a spring when closed. To open the injector, current is passed through the solenoid coil, generating a magnetic field which creates vertical force on the armature, causing the entire valve needle assembly to lift. If the solenoid armature is still in motion from the closing of a previous injection when a subsequent injection begins, significant nonlinearity in total fuel quantity may be observed as dwell time between injections is modified. Additionally, the armature may bounce upon closing, resulting in unintended fuel delivery.

Several methods have been developed to reduce nonlinearity and/or armature bounce, including optimization of the electromagnetic geometry [5], armature mass reduction [6], non-rigid coupling of the armature to the needle [7], and modulation of the current waveform [7, 8]. Measurement of motions of the internal components is critical to understanding and improving injectors. The most common measurement of interest is the axial motion, or lift, of the armature and/or valve needle. Armature lift can be measured by using the solenoid itself as a sensor by analysis of the voltage and current waveforms [9]. Needle lift at the top of the needle has been measured by laser Doppler vibrometry [10], and lift and wobble (radial motion) of the check ball have been observed via optically transparent nozzles [11, 12] and x-ray imaging [13, 14]. However, it is not possible to make an entire injector optically transparent due to the high fuel pressure, and the thick metal cross section of the solenoid makes x-ray imaging challenging. A full accounting of the internal dynamics of injectors has not yet been achieved.

Unlike photons, which interact primarily with the electrons in matter, neutrons interact primarily with atomic nuclei, and therefore have high penetration through most materials including many metals. Neutron interactions are isotope-specific, and ^{1}H has a particularly high incoherent scattering cross section, which means that neutrons are sensitive to any hydrogenous material, including hydrocarbon fuel. This makes neutron imaging an ideal tool for studying the fluid and mechanical dynamics inside fuel injectors, as neutrons can easily penetrate the metal injector while having high contrast to the liquid fuel inside. In recent work, we demonstrated that high-speed neutron imaging could resolve oscillatory motions of an injector needle on the order of 5 μm at 5 μs time scale [15]. However, the field of view in that effort was restricted to only the very end of the needle near the valve ball. In this work, we extend the field of view to cover the entire injector, offering a complete picture of the internal mechanical dynamics while simultaneously imaging the internal and external fluid dynamics.

2. Experimental setup

2.1 Neutron imaging

High-speed neutron imaging was performed at the CG-1D cold neutron imaging beamline [16] at the High Flux Isotope Reactor (HFIR), a Department of Energy user facility operated by the Oak Ridge National Laboratory (ORNL). A ^{10}B-doped microchannel plate (MCP) detector with 2 × 2 Timepix readout was used. The MCP detector has 512 × 512 pixels with 2.8 × 2.8 cm field of view, a physical pixel size of 55 μm, and 1 μs timing capability [17]. The instrument has an adjustable aperture, which was set to 16 mm, and a fixed aperture-to-detector distance of 6.59 m, resulting in an L/D ratio of 412.

One of the biggest challenges with neutron imaging of dynamic processes is the relatively low flux of neutrons. Single-shot measurements of dynamics inside injectors, which occur at μs to ms timescales, are not possible with existing neutron sources. However, high temporal resolution can still be achieved by making cyclic ensemble measurements. In this case, we operated the injector in synchronization with the MCP detector at an injection frequency of 50 Hz to make ensembles consisting of ~5–6×10^6 injection events for each movie. As described in previous work [15], ensemble image sequences were acquired in a series of shutters with time bin sizes ranging from 5.12 μs to 20.48 μs. The raw data, which is in the form of neutron counts per pixel per time bin, were overlap corrected [18], re-binned to 20.48 μs (equivalent to 48,828 frames/s), and normalized to count rate to account for the variation in number of successfully acquired shutters. The resulting image sequences were further processed with a 10 kHz, zero-phase, second-order Butterworth lowpass filter in the temporal domain.

2.2 Spray rig

An 8-hole gasoline direct injector was mounted in a spray rig developed specifically for neutron imaging, pictured in **Figure 2**. The inlet of the injector was connected to a heated fuel rail via a high-pressure rotary union, and a rotation mount with a custom adapter allowed the injector to be rotated precisely to any desired angle. The outlet of the injector was fitted into a thin-walled aluminum tube, which is highly transparent to neutrons. The aluminum tube was connected to a stainless steel tee fitting which was continuously purged with nitrogen gas at a fixed rate provided by a mass flow controller. A pilot-operated backpressure valve located downstream of the tee controlled the pressure of the environment inside the aluminum tube.

The spray rig was mounted on a 3-axis positioning stage at the CG-1D instrument. The stage allowed the injector to be positioned directly in front of the MCP detector and allowed for translation of the injector to different positions, at it is too large to fit entirely within the field of view of the detector. Boron impregnated rubber was used to shield all parts of the spray rig except for the injector itself, which was open to air in order to provide an unobstructed view for the neutron beam, as shown in **Figure 2C**. All connections to the spray rig, including fuel supply, sweep gas supply, exhaust vacuum line, and electrical signals were made with flexible hoses and wiring in order to allow unimpeded movement of the spray rig on the positioning stage.

A diagram of the gas flow path is shown in **Figure 3**. The majority of the equipment for the experiment was located outside of the instrument radiation shielding, denoted as “cage” in **Figure 3**, to minimize neutron activation. The nitrogen sweep gas was provided by cryogenic cylinders located outside of the building on a gas manifold to enable seamless switching between cylinders. After passing through the mass flow controller, the nitrogen passed through a flexible heated hose before entering the spray rig, which allowed for control of the gas temperature downstream of the injector. All components downstream of the mixing tee, including the backpressure regulator and the exhaust vacuum line, were heated to prevent condensation of fuel in the exhaust flow path, which passed out of the instrument and into a fuel recovery system. This system used a cold trap operated at −45 °C to condense the fuel out of the exhaust. The recovered fuel was then returned to the fuel system, which operated in a closed loop to minimize fuel quantity in the building.

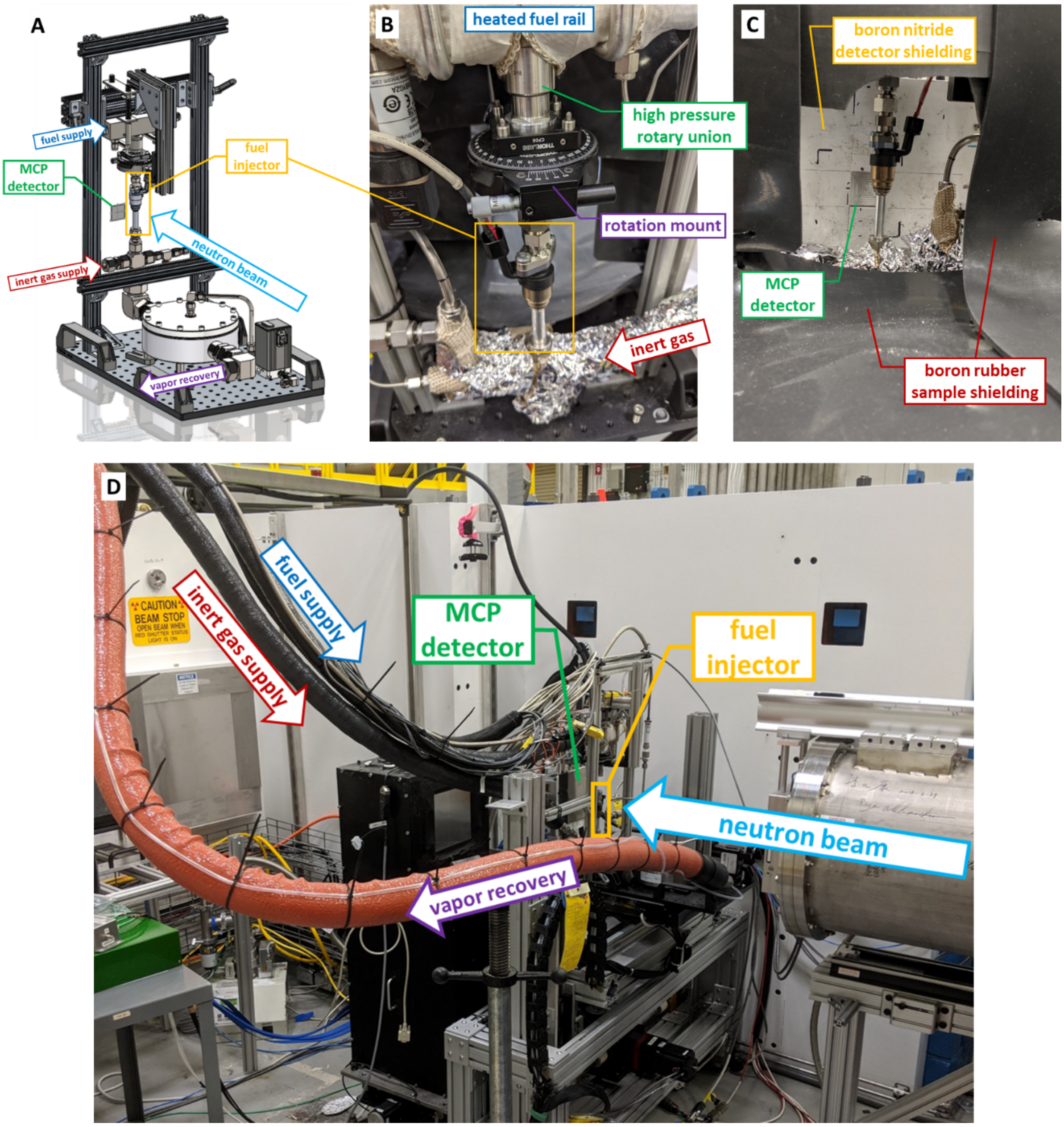

Figure 2. Experimental setup. **A:** Model of the injector spray rig. **B:** View of spray rig from behind. **C:** View of spray rig from front (approximate neutron perspective). **D:** Spray rig installed at CG-1D on 3-axis positioning stage

2.3 Operating conditions

The injector was operated at 50 Hz with a single injection per cycle and a commanded duration of 680 µs per injection. The fuel was iso-octane (C_8H_{18}, 2,2,4-trimethylpentane) and was supplied at 200 bar and 90 °C. The nitrogen sweep gas was supplied at 60 °C, and pressure downstream of the injector was maintained at 100 kPa to emulate conditions of injection early in the compression stroke of a GDI engine.

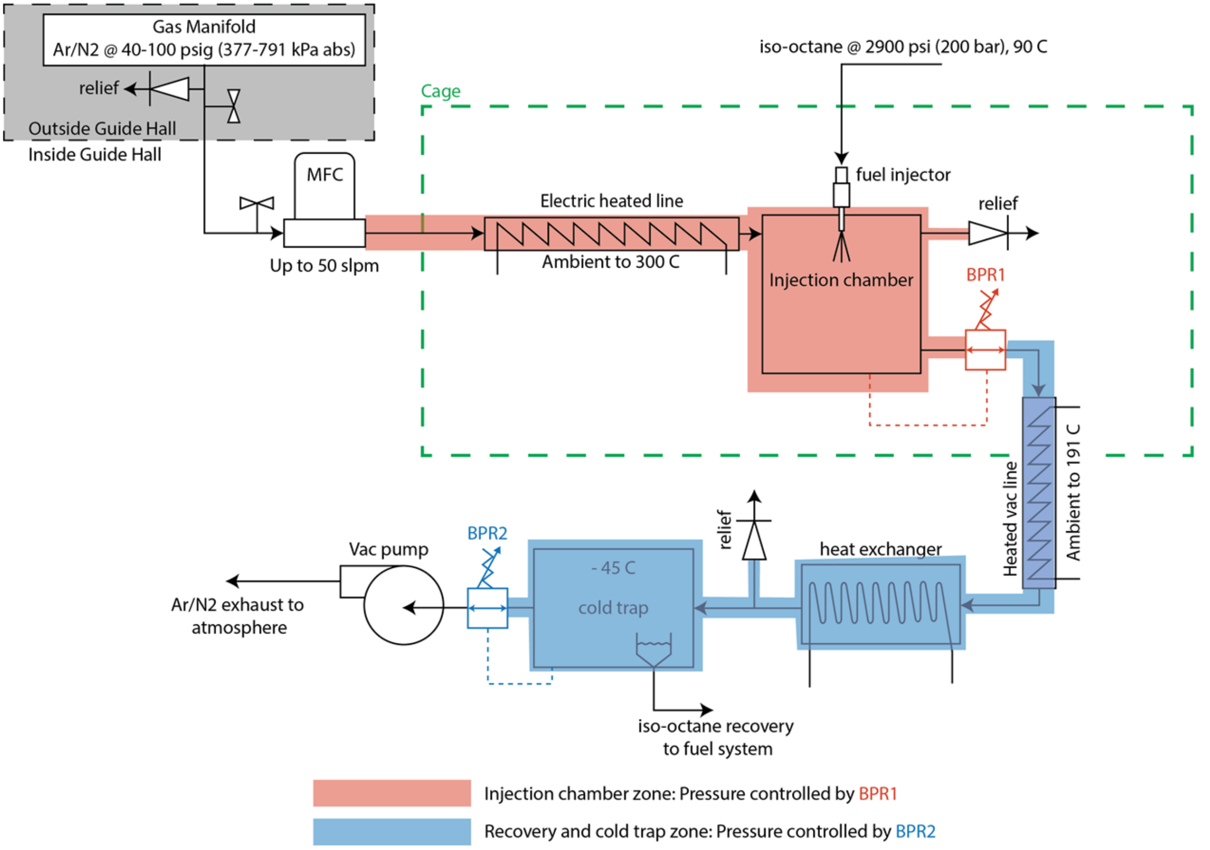

Figure 3. Spray rig gas flow path and fuel recovery diagram

3. Methodology

Neutron imaging is a form of transmission radiography. As a neutron beam passes through a sample, it is attenuated according to the Beer–Lambert law:

$$T = \frac{I}{I_0} = e^{-\Sigma d} \tag{1}$$

Here I_0 is the incident intensity, I is the transmitted intensity, Σ is the macroscopic attenuation coefficient, and d is the path length. For a sample comprised of multiple materials or phases (A, B, C, …),

$$T = \frac{I}{I_0} = e^{-(\Sigma_A d_A + \Sigma_B d_B + \Sigma_C d_C + \cdots)} \tag{2}$$

where each phase may have a different attenuation coefficient and path length. An example of a neutron transmission image for the fuel injector used in this study is shown in **Figure 4**. As shown in **Figure 4A**, the field of view of the MCP detector does not cover the entire injector; therefore the injector was translated to three different positions, and the resulting images were stitched together to produce the linear-scaled transmission image in **Figure 4B** and the log-scaled transmission image in **Figure 4C**. Because the injector was filled with fuel, which strongly attenuates neutrons, the inside of the injector appears almost black in the linear-scaled image. However, due to the high contrast between fuel and steel, the internal components become visible when presented in log scale.

For the stitched transmission image in **Figure 4**, each of the three positions was normalized against an “open beam” (I_0) image in which no sample is present. All images were acquired with 60 s exposure time. In principle, this same normalization approach could be used in high-speed imaging. However, much of the dynamic behavior inside the injector occurs at length scales below the 55 μm pixel size of the MCP detector and will not be readily apparent in a transmission image. To overcome this, we instead normalize our high-speed image sequence against a frame or set of frames from the same sequence.

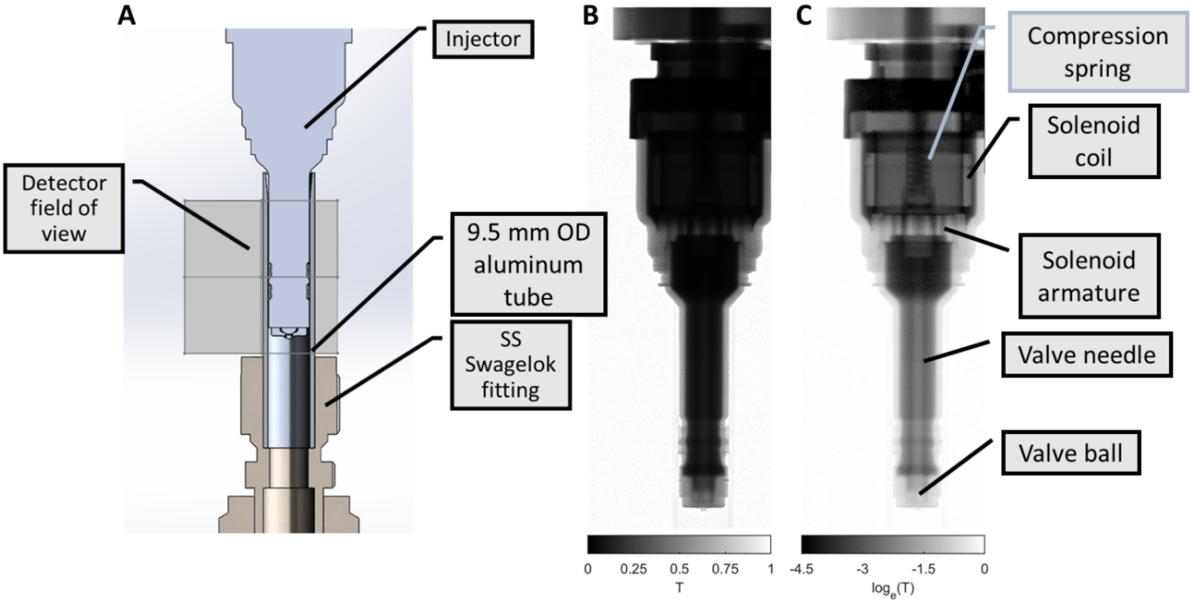

Figure 4. A: Detector field of view compared to injector model. **B:** Linear-scaled transmission image of stitched radiographs. **C:** Log-scaled transmission image reveals internal features of injector

As described in our previous work [15], this results in an image

$$\frac{I(t)}{I_{\text{ref}}} = e^{-[\Sigma_A(d_A(t)-d_{A,\text{ref}})+\Sigma_B(d_B(t)-d_{B,\text{ref}})+\Sigma_C(d_C(t)-d_{C,\text{ref}})+\cdots]} \tag{3}$$

which essentially represents how the path lengths through each phase have changed in the dynamic image $I(t)$ compared to the reference image I_{ref}, weighted by the attenuation coefficient of each phase. This can be simplified by assuming that there are only two moving phases. For our injector, these may be the armature (phase A) and the fuel around the armature (phase B). If we assume that the housing of the injector (phase C) is static, then the distance that a given neutron must travel through the housing and the air around the housing will be the same in both the dynamic and reference images, so all the path length difference terms other than A and B will drop out in Equation (3). This assumption also means that the total length through A and B is conserved:

$$d_{A,\text{ref}} + d_{B,\text{ref}} = d_A(t) + d_B(t) \tag{4}$$

By substituting Equation (4) into Equation (3) and taking the natural logarithm, we obtain

$$\log_e\left(\frac{T(t)}{T_{\text{ref}}}\right) = (\Sigma_B - \Sigma_A)(d_A(t) - d_{A,\text{ref}}) \tag{5}$$

This image is a map of how the path length through phase A changed, scaled by the attenuation coefficient difference between the phases A and B. This image can then be analyzed according to the approach described in our previous work [15], in which the geometry and attenuation coefficients of the internal components of the injector are extracted from a neutron CT scan and are then used to create a model of how the path length seen by each pixel on the detector would change if the geometry were displaced by a given amount. This model can then be fit to the log-normalized image described in Equation (5) to estimate the displacement that best fits the data.

The geometry of the solenoid armature and the valve ball were modelled based on the CT scan of the injector shown in **Figure 1**. Two-dimensional path length models were developed for each following the approach described in our previous work [15]. The models are illustrated in **Figure 5**, with the armature displaced horizontally by 0.25 px and vertically by 0.5 px, and the valve ball displaced horizontally by 0.1 px and vertically by 0.5 px. The distance maps of the reference and displaced geometry are visually indistinguishable, but in the distance difference map, the displacement is readily apparent. Note that the distance difference $d(t) - d_{\text{ref}}$ is an order of magnitude larger for the armature than the valve ball due to the steep gradient in path length at the edges of the armature. For simplicity, the internal holes in the armature shown in **Figure 1** have been ignored, with the armature modeled as a solid body. This is addressed by fitting only the edges of the armature to the data.

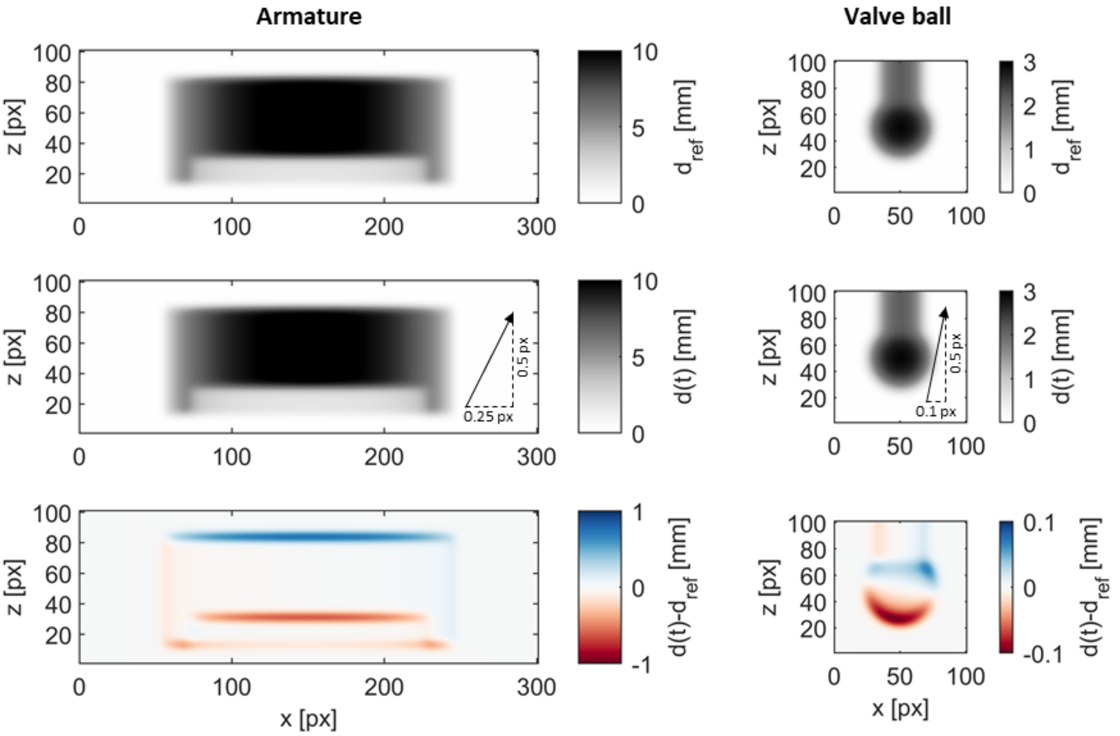

Figure 5. Path length models for solenoid armature and valve ball

Attenuation coefficients were extracted from the neutron CT scan and are shown in **Table 1**. The values measured within the solid components (Σ_A) are effectively constant, whereas the values for the fuel surrounding the components (Σ_B) will vary with path length due to beam hardening, as discussed in our previous work [15]. There it was shown that selecting a representative value of Σ_B based on the average path length produces good results, but there is uncertainty in the fit due to uncertainty in the absolute value of Σ_B, which is affected not only by beam hardening by also by incoherent scattering, which will vary with sample-to-detector distance. Here we have included upper and lower bounds on Σ_B based on the path length range in each component to provide an estimate of the uncertainty in the fit.

Table 1. Attenuation coefficients used in model. Upper and lower bounds for fuel attenuation coefficient due to beam hardening shown in parentheses

Component	Solid: Σ_A [cm^{-1}]	Fuel: Σ_B [cm^{-1}]	$\Sigma_B - \Sigma_A$ [cm^{-1}]
Solenoid armature	0.6	4.1 (3.71, 4.49)	3.50 (3.11, 3.89)
Valve ball	1.0	4.24 (3.99, 4.49)	3.24 (2.99, 3.49)

4. Results and discussion

Selected images from the high-speed image sequence are shown in **Figure 6**. The injector was imaged in two positions to cover the region of interest. The upper position, which includes the solenoid, was formed as the ensemble of 6.38×10^6 injection events, while the lower region, which includes the valve ball and spray, was formed as the ensemble of 4.89×10^6 injection events. The two regions overlap by ~3 mm and were not stitched together in the images shown. The sequence is displayed using two normalization approaches, both of which use a reference image generated by taking the median of the 10 images immediately preceding start of energization (SOE). The first normalization, shown in a sequential black and white colormap, is formed by subtracting 95% of the reference image I_{ref} from the time series image $I(t)$, and is purely qualitative in that it allows for visualization of the changes in intensity while preserving a faint image of the injector. The second normalization, shown in a diverging red, white, and blue colormap, is the log-ratio described in Equation (5) and was used to perform the model fits of the solenoid armature and valve ball displacement.

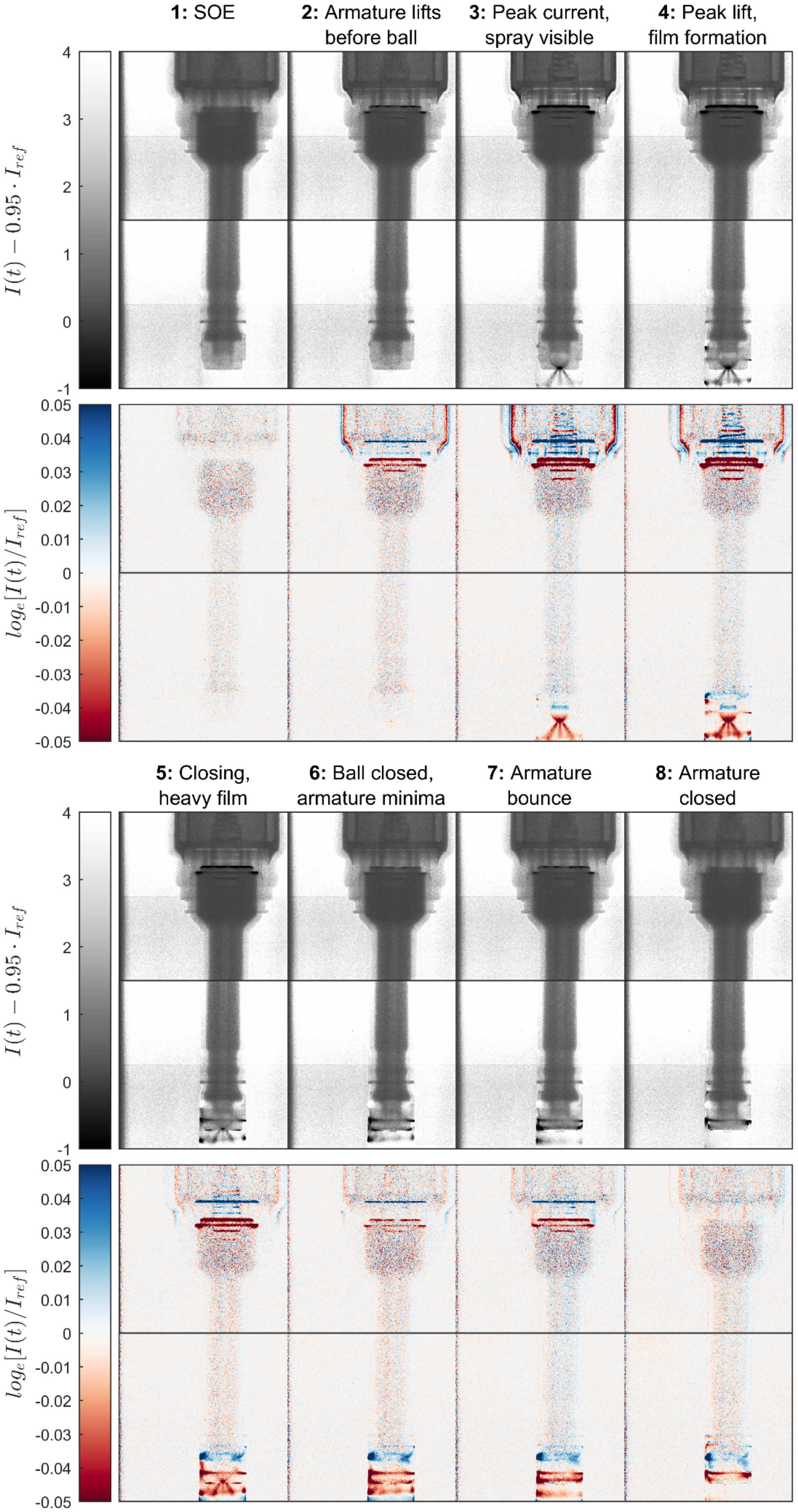

Figure 6. Normalized high-speed neutron images of gasoline direct injector dynamics

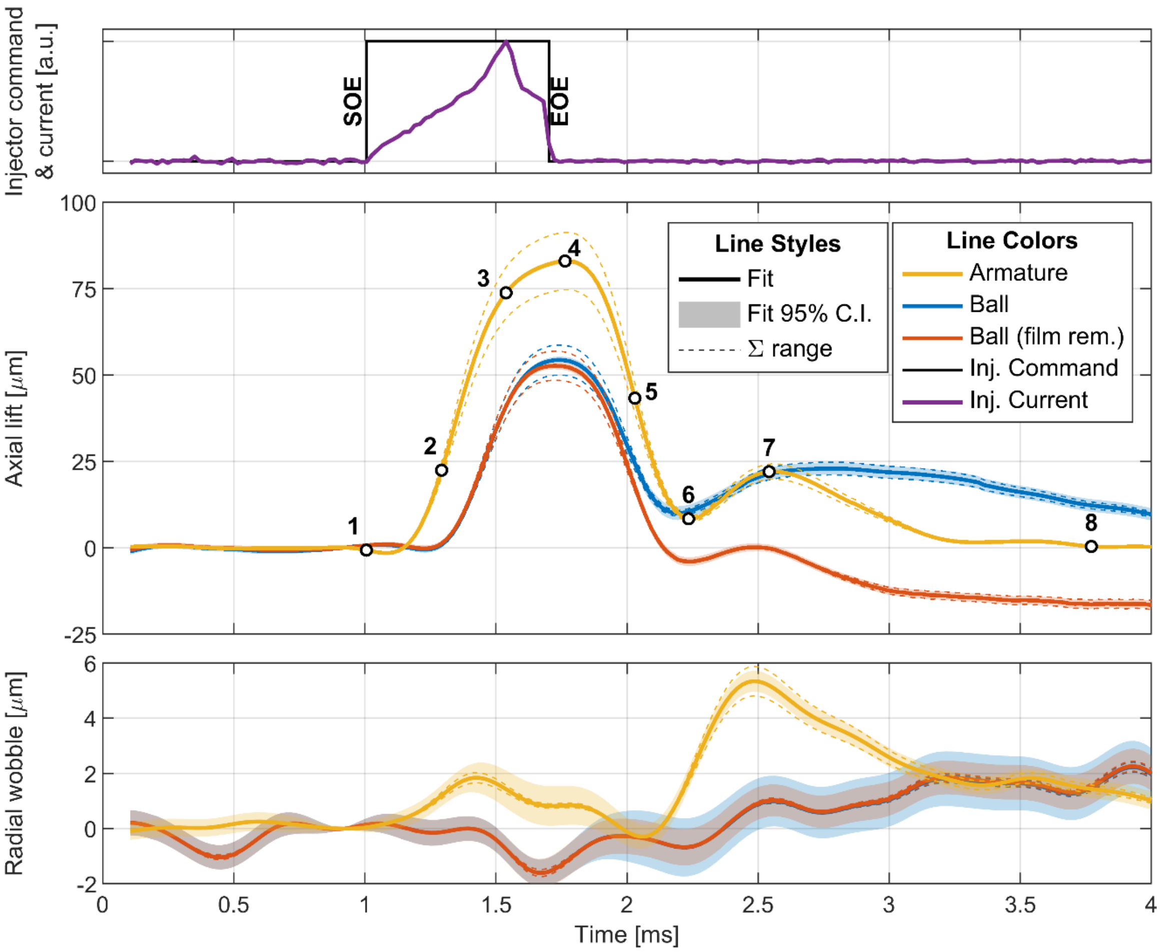

Figure 7. Results of solenoid armature and valve ball displacement model fitting

The injector energization command and current profile, and the fits of axial lift and radial wobble of the solenoid armature and valve ball are shown in **Figure 7** with annotations corresponding to the selected images shown in **Figure 6**. The shaded region behind each curve corresponds to the 95% confidence interval associated with the displacement model fit, while the dashed lines correspond to the range due to uncertainty in the attenuation coefficients. There are several results of note:

Image 1 (1.00 ms): At SOE, the log-ratio image is flat, indicating no change relative to the reference image. However, note the presence of increased noise within the injector, where the total neutron count rates are lower due to their passage through the strongly attenuating fuel.

Image 2 (1.29 ms): The armature lifts 22 μm before any motion is observed in the valve ball. This is presumed to be due to the long valve needle, which can deflect slightly to store compressive energy much like a spring. Variations are also observed in the housing around the solenoid.

Image 3 (1.54 ms): At peak injector current, the armature lift is 74 μm, while the valve ball lift is 41 μm. The fuel spray plumes can be seen emanating from the nozzle holes, and the motion of the compression spring above the armature is also visible. The variations in the solenoid and housing are now stronger and will be discussed subsequently.

Image 4 (1.76 ms): Peak lift occurs just after end of energization (EOE), with armature lift reaching 83 μm and valve ball lift reaching 52 to 55 μm. The spray plumes can be seen impinging on the inner surface of the aluminum tube, and fuel film is developing around the tip of the injector, as indicated by the horizontal red bands in the log-ratio image.

Image 5 (2.03 ms): Both the armature and valve ball are closing, and heavy film development can be seen around the injector tip. The location of impingement on the aluminum tube has also climbed up due to a low-pressure recirculation zone behind the spray. The blue horizontal band above the valve ball indicates that a fuel film which was present in the reference image has been pulled down to the location indicated by the red horizontal band centered on the valve ball. The presence of this film interferes with the valve ball displacement model, and an additional fit is shown in **Figure 7** by the red curve in which the film has been (partially) removed from the images, as described in the next section.

Image 6 (2.23 ms): The valve ball is now completely closed, and no spray is seen. However, the armature does not close, but reaches a minimum lift of 8 μm.

Image 7 (2.54 ms): The armature bounces back up to 22 μm and shifts to the right by 5 μm. The valve ball fit performed on the image with fuel film indicates a lift of 21 μm, but no spray is visible in the image, and this is believed to be a spurious result. The valve ball fit performed on the image with the fuel film removed indicates ~0 μm lift. Heavy bands of fuel film are seen both around the injector tip and the inner circumference of the aluminum tube.

Image 8 (3.77 ms): The armature settles rather slowly, requiring 1.54 ms to fully close after reaching its initial minimum in Image 6. The fuel films continue to slowly dissipate beyond this point.

While not readily apparent in these still images, the valve needle can also be seen to oscillate during injection when the image sequence is played as a movie.

Examples of the solenoid armature and valve ball fits are shown in **Figure 8**. Because the internal features of the armature were not modeled, the center of the armature was ignored in the fit, which used only the sides and the bottom edge to compute displacement. Similarly, the sac volume below the valve ball involves three phases (valve ball, fuel, nitrogen) and was cropped out of the images used in the valve ball displacement fits. As shown in **Figure 8**, the armature fit to image 7 and the ball fit to image 3 both do an excellent job of matching the data, leaving little if any structure in the residual. However, once fuel films begin to develop around the outside of the injector tip, they interfere with the valve ball fit, as seen in the fit of image 5. This was accounted for by developing a model which assumes that a horizontally symmetric film of constant radius exists in the image, and then fitting the radius and film thickness to the data one line at a time, as shown for image 5 in **Figure 8**. This approach does remove much of the film from the image, but there are artifacts in the residual image due to the asymmetry of the film. As shown in **Figure 7**, this approach does remove the positive bias in the valve ball lift beyond 2 ms but ends up resulting in a negative bias beyond 2.5 ms. The presence of the film and the associated higher noise in that region of the image is likely also the reason for the slowly increasing fitted value of ball radial wobble beyond 2 ms. The best approach to deal with the fuel film would be to seal the end of the injector in the tube so that film cannot develop around the injector, but that was beyond the scope of this work.

The variations observed in the solenoid during energization in **Figure 6** merit further discussion. Neutrons have a magnetic moment and will undergo precession at the Larmor frequency when passing through a magnetic field. This property can be used to enable imaging and tomography of magnetic fields by spin-polarizing the neutron beam [19, 20]. However, because neutrons do not have charge, their trajectory is not altered by passing through a magnetic field, and because we are using unpolarized neutrons, there should be no change in total neutron count rate due to interaction with the magnetic fields in the energized solenoid.

When the coil is energized, a magnetic field develops around the coil, which passes through the magnetic core, the external housing, and the armature [7], as illustrated in **Figure 1**. This field creates both axial and radial forces within the coil, which tend to compress the coil in the axial direction and expand the coil in the radial direction [21]. Additionally, the electrical resistance of the coil leads to Joule heating which in turn causes thermal expansion of the coil [22]. Cyclic compressive stresses and high temperature can lead to degradation of the insulation between the coil wires, which is the leading cause of solenoid failure. The normalized images 2, 3, and 4 of **Figure 6** show the entire coil, magnetic core, and housing expanding radially outward. Though not pursued in this work, quantitative analysis of this expansion could be a valuable tool for validation of finite element models investigating solenoid lifetime and reliability.

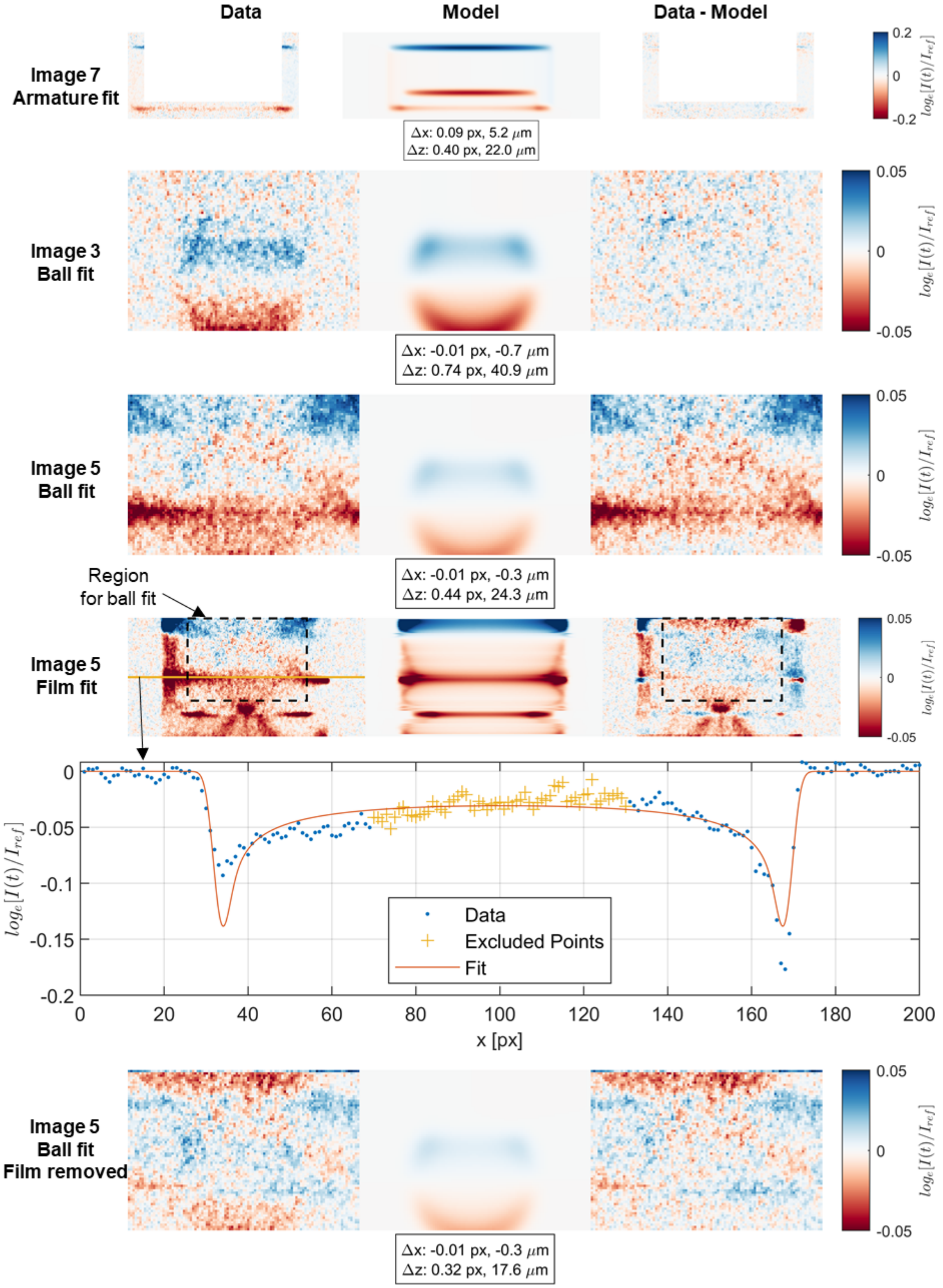

Figure 8. Example fits for the solenoid armature and valve ball displacement models and wall film model

5. Conclusions

We have demonstrated that high-speed neutron imaging can enable visualization of the internal mechanical dynamics of an entire gasoline direct injector, and our recently developed attenuation model allows for the quantification of motions of components such as the solenoid armature and valve ball at subpixel scales of the order of 1 μm in both axial and radial directions. It is also possible to see dynamics such as the swelling of the solenoid during energization, the development of the fuel spray both inside and outside the injector, fuel impingement on internal surfaces, and the development and transport of fuel films, all through solid metal components. Future prospects for this approach may include validation of electromagnetic and hydromechanical models of solenoid actuators and visualization of hydrogenous sprays and films inside dense metallic objects such as internal combustion engines, oil-lubricated compressors, multi-phase heat exchangers, and many other applications [23].

Acknowledgements

The authors acknowledge the contributions of Anton Tremsin at the UC Berkeley Space Sciences Laboratory to the development of the high-speed imaging capability with the MCP detector, Jonathan Willocks at ORNL for assistance with the development of the spray apparatus and execution of the experiments, Scott Parish and Ronald Grover at General Motors for providing the injector and injector driver, and DOE program managers Gurpreet Singh and Michael Weismiller for their support.

This work was supported by the US Department of Energy, Office of Energy Efficiency and Renewable Energy, Vehicle Technologies Office via the Advanced Combustion Engine Systems program. This research used resources at the High Flux Isotope Reactor, a DOE Office of Science User Facility, and the National Transportation Research Center, a DOE Office of Energy Efficiency and Renewable Energy User Facility, both operated by the Oak Ridge National Laboratory.

The authors declare no competing interests.

References

1. *The 2021 EPA Automotive Trends Report: Greenhouse Gas Emissions, Fuel Economy, and Technology since 1975*. 2021 [cited 2022 May]; Available from: https://www.epa.gov/automotive-trends.
2. Myung, C.L. and S. Park, *Exhaust nanoparticle emissions from internal combustion engines: A review.* International Journal of Automotive Technology, 2011. **13**(1): p. 9. DOI: https://doi.org/10.1007/s12239-012-0002-y.
3. Raza, M., et al., *A Review of Particulate Number (PN) Emissions from Gasoline Direct Injection (GDI) Engines and Their Control Techniques.* Energies, 2018. **11**(6): p. 1417. DOI: https://doi.org/10.3390/en11061417.
4. Duke, D.J., et al., *High-resolution x-ray and neutron computed tomography of an engine combustion network spray G gasoline injector.* SAE International Journal of Fuels and Lubricants, 2017. **10**(2): p. 328-343. DOI: https://doi.org/10.4271/2017-01-0824.
5. Shin, Y., et al., *Shape optimization to minimize the response time of direct-acting solenoid valve.* Journal of magnetics, 2015. **20**(2): p. 193-200. DOI: https://doi.org/10.4283/JMAG.2015.20.2.193.
6. Passarini, L. and P. Nakajima, *Development of a high-speed solenoid valve: an investigation of the importance of the armature mass on the dynamic response.* Journal of the Brazilian Society of Mechanical Sciences and Engineering, 2003. **25**(4): p. 329-335. DOI: https://doi.org/10.1590/S1678-58782003000400003.
7. Kusakabe, R., et al., *Injection Quantity Range Enhancement by Using Current Waveform Control Technique for DI Gasoline Injector.* SAE International Journal of Engines, 2014. **7**(2): p. 560-567. DOI: https://doi.org/10.4271/2014-01-1211.
8. Skiba, S. and J. Melbert, *Dosing Performance of Piezo Injectors and Sensorless Closed-Loop Controlled Solenoid Injectors for Gasoline Direct Injection.* SAE International Journal of Engines, 2012. **5**(2): p. 330-335. DOI: https://doi.org/10.4271/2012-01-0394.
9. Koch, A., H. Glasmachers, and J. Melbert, *Sensorless Movement Control of Solenoid Fuel Injectors*. 2006, SAE International. DOI: https://doi.org/10.4271/2006-01-0407.
10. Cavicchi, A. and L. Postrioti, *Simultaneous needle lift and injection rate measurement for GDI fuel injectors by laser Doppler vibrometry and Zeuch method.* Fuel, 2021. **285**: p. 119021. DOI: https://doi.org/10.1016/j.fuel.2020.119021.
11. Mamaikin, D., et al. *High speed shadowgraphy of transparent nozzles as an evaluation tool for in-nozzle cavitation behavior of GDI injectors*. in *Ilass Europe. 28th european conference on Liquid Atomization*

and Spray Systems. 2017. Editorial Universitat Politècnica de València. DOI: http://dx.doi.org/10.4995/ILASS2017.2017.4639.
12. Mamaikin, D., et al., *Experimental investigation of flow field and string cavitation inside a transparent real-size GDI nozzle.* Experiments in Fluids, 2020. **61**(7): p. 154. DOI: https://doi.org/10.1007/s00348-020-02982-y.
13. Baldwin, E.T., et al., *String flash-boiling in gasoline direct injection simulations with transient needle motion.* International Journal of Multiphase Flow, 2016. **87**: p. 90-101. DOI: https://doi.org/10.1016/j.ijmultiphaseflow.2016.09.004.
14. Pratama, R.H., et al., *Hydraulic flip in a gasoline direct injection injector and its effect on injected spray.* Fuel, 2022. **310**: p. 122303. DOI: https://doi.org/10.1016/j.fuel.2021.122303.
15. Wissink, M.L., et al., *Quantification of Sub-Pixel Dynamics in High-Speed Neutron Imaging.* Journal of Imaging, 2022. **8**(7): p. 201. DOI: https://doi.org/10.3390/jimaging8070201.
16. Santodonato, L., et al., *The CG-1D Neutron Imaging Beamline at the Oak Ridge National Laboratory High Flux Isotope Reactor.* Physics Procedia, 2015. **69**: p. 104-108. DOI: https://doi.org/10.1016/j.phpro.2015.07.015.
17. Tremsin, A.S., et al., *Detection efficiency, spatial and timing resolution of thermal and cold neutron counting MCP detectors.* Nuclear Instruments and Methods in Physics Research Section A: Accelerators, Spectrometers, Detectors and Associated Equipment, 2009. **604**(1): p. 140-143. DOI: https://doi.org/10.1016/j.nima.2009.01.041.
18. Tremsin, A.S., et al., *Optimization of Timepix count rate capabilities for the applications with a periodic input signal.* Journal of Instrumentation, 2014. **9**(05): p. C05026. DOI: http://dx.doi.org/10.1088/1748-0221/9/05/C05026.
19. Kardjilov, N., et al., *Imaging with Polarized Neutrons.* Journal of Imaging, 2018. **4**(1): p. 23. DOI: https://doi.org/10.3390/jimaging4010023.
20. Hilger, A., et al., *Tensorial neutron tomography of three-dimensional magnetic vector fields in bulk materials.* Nature Communications, 2018. **9**(1): p. 4023. DOI: https://doi.org/10.1038/s41467-018-06593-4.
21. Hao, S. and B. Li, *Calculating the magnetic force of solenoid inductor wound by rectangular cross-section wire.* IET Electric Power Applications, 2021. **15**(9): p. 1154-1160. DOI: https://doi.org/10.1049/elp2.12085.
22. Angadi, S.V., et al., *Reliability and life study of hydraulic solenoid valve. Part 1: A multi-physics finite element model.* Engineering Failure Analysis, 2009. **16**(3): p. 874-887. DOI: https://doi.org/10.1016/j.engfailanal.2008.08.011.
23. Craster, R.V. and O.K. Matar, *Dynamics and stability of thin liquid films.* Reviews of Modern Physics, 2009. **81**(3): p. 1131-1198. DOI: https://doi.org/10.1103/RevModPhys.81.1131.